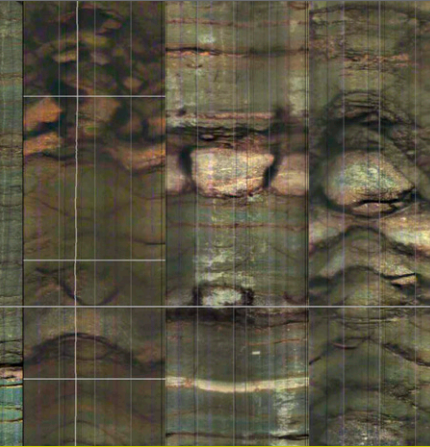


Brad W. Kuntz\*  
Shira Rubin  
Brian Berkowitz  
Kamini Singha



We quantify solute transport in geologic media with the mobile-immobile and continuous-time random walk models. Breakthrough curves from soil cores and a field-scale tracer experiment reveal anomalous early breakthrough and long tailing. Transport is controlled by preferential flow pathways, the abundance of rock fragments, and soil weathering.

B.W. Kuntz and K. Singha, Dep. of Geosciences, Pennsylvania State Univ., University Park, PA 16802; and S. Rubin and B. Berkowitz, Dep. of Environmental Sciences and Energy Research, Weizmann Institute of Science, Rehovot 76100, Israel. \*Corresponding author (bkuntz@psu.edu).

Vadose Zone J. 10:843–857  
doi:10.2136/vzj2010.0130  
Received 29 Oct. 2010.  
Posted online 29 July 2011.

© Soil Science Society of America  
5585 Guilford Rd., Madison, WI 53711 USA.  
All rights reserved. No part of this periodical may be reproduced or transmitted in any form or by any means, electronic or mechanical, including photocopying, recording, or any information storage and retrieval system, without permission in writing from the publisher.

# Quantifying Solute Transport at the Shale Hills Critical Zone Observatory

We collected and analyzed Br<sup>-</sup> breakthrough curve (BTC) data to identify the parameters controlling transport from a series of soil cores and a field-scale tracer test at the Shale Hills Critical Zone Observatory (SH-CZO) in central Pennsylvania. The soil cores were retrieved from a continuous hole that extended through the soil profile to quantify also how solute transport behavior changes with depth and weathering. Additionally, we performed a field-scale doublet tracer test to determine transport behavior in the weathered shale bedrock. Hydraulic conductivity and porosity were as low as 10<sup>-15</sup> m s<sup>-1</sup> and 0.035, respectively, in the shale bedrock and upward of 10<sup>-5</sup> m s<sup>-1</sup> and 0.45, respectively, in the shallow soils. Bromide BTCs demonstrated significant tailing in soil cores and field tracer experiments, which does not fit classical advection–dispersion processes. To quantify the behavior, numerical simulation of solute transport was performed with both a mobile–immobile (MIM) model and a continuous-time random walk (CTRW) approach. One-dimensional MIM modeling results yielded low mass transfer rates (<1 d<sup>-1</sup>) coupled with large immobile domains (immobile/mobile porosity ratio of 1.5–2). The MIM modeling results also suggested that immobile porosity was a combination of soil texture, fractures, and porosity development on shale fragments. One-dimensional CTRW results yielded a parameter set indicative of a transport regime that is consistently non-Fickian within the soil profile and bedrock. These modeling results confirm the important role of preferential flow paths, fractures, and mass transfer between more- and less-mobile fluid domains and advance the need to incorporate a continuum of mass transfer rates to more accurately quantify transport behavior within the SH-CZO.

Abbreviations: ADE, advection–dispersion equation; BTC, breakthrough curve; CTRW, continuous-time random walk; MIM, mobile–immobile; pdf, probability density function; PSD, particle size distribution; SH-CZO, Shale Hills Critical Zone Observatory; TPL, truncated power law.

**The SH-CZO** has been developed as a natural laboratory to predict the creation and function of regolith within a multidisciplinary context. The flow of water and transport of solutes within this catchment are key to dating groundwater, estimating soil weathering rates, predicting nutrient availability, classifying primary and secondary fluid pathways, and identifying controls on the residence time of solutes in the subsurface (Amundson et al., 2007; Brantley et al., 2007; Anderson et al., 2008; Dere et al., 2010). Identifying groundwater age is a useful means to investigate watershed-scale processes including discharge and recharge areas, preferential flow paths, and drought vulnerability or resource protection (Kazemi et al., 2006). Calculating groundwater ages has traditionally been accomplished by advection-only models (e.g., Reilly et al., 1994), although the importance of dispersion and diffusion processes is well recognized (e.g., Goode, 1996; Varni and Carrera, 1998; Bethke and Johnson, 2008). Recent models, such as those described in Duffy (2010), incorporate the diffusion of solutes between dead-end pore space and the advective fluid domain; however, data are required to (i) constrain the residence times of fluids within these more- and less-mobile domains, and (ii) evaluate the distribution of the pore space within the subsurface. This study provides data for these two requirements and explores the assumptions within conceptual transport models at the SH-CZO.

Classically, transport is described by the advection–dispersion equation (ADE). With the ADE, the shape of the breakthrough history is fitted by estimating the dispersivity (e.g., Koch and Flühler, 1993; Perfect et al., 2002; Javaux and Vanclooster, 2003; Vanderborght and Vereecken, 2007); however, the assumption of Fickian transport intrinsic in the ADE prevents its ability to effectively predict and characterize solute transport behavior in heterogeneous environments (e.g., Adams and Gelhar, 1992; Silliman and Simpson, 1987; Huang et al., 1995; Javaux and Vanclooster, 2004; Gorelick et al., 2005).

Of particular interest in this work was an evaluation of the physical processes trapping solutes in immobile pore space, the matrix, or less-mobile pathways. The SH-CZO's regolith and bedrock are dominated largely by silty-loam soils and fractured shale bedrock that are likely to contain significant immobile pore space (Lin, 2006). The presence of immobile pore space has been documented in many geologic materials and scales ranging from well-sorted sandstone (e.g., Coats and Smith, 1964) to saprolitic soils (e.g., Gwo et al., 2007) and fractured bedrock (e.g., Jardine et al., 1999). Fundamental to quantifying transport within these materials is a sufficient accounting of scale-dependent processes including dispersion, diffusion, and mass transfer. Incorporating the transfer of mass between less-mobile pore space and the mobile pore space has facilitated improved fitting of BTCs in many settings where long concentration tailing behavior is seen (e.g., van Genuchten and Wierenga, 1976; Cameron and Klute, 1977; Seyfried and Rao, 1987; Haggerty and Gorelick, 1994; Maraqa et al., 1997; Jardine et al., 1999; Gao et al., 2009). We followed the approach of Gao et al. (2009) to compare alternative conceptual and numerical models to constrain, predict, and interpret solute transport behavior. We inspected a well-characterized catchment by performing tracer experiments in the laboratory and field to interpret solute transport behavior given two different conceptual transport models of varying complexity.

## Conceptual Models of Solute Transport

Recognition that heterogeneous environments contain fast and slow paths (fracture and matrix, mobile and immobile zones, or preferential pathways and dead-end pore space) advocated the development of alternative transport models to the ADE. One simple model is the MIM model (van Genuchten and Wierenga, 1976), shown here in one dimension:

$$\theta_m \frac{\partial c_m}{\partial t} + \theta_{im} \frac{\partial c_{im}}{\partial t} = \theta_m D \frac{\partial^2 c_m}{\partial x^2} - v_m \theta_m \frac{\partial c_m}{\partial x} \quad [1]$$

where  $\theta$  is the porosity ( $\text{cm}^3 \text{cm}^{-3}$ ),  $c$  is the concentration of the solute [ $\text{M L}^{-3}$ ],  $v_m$  is the average fluid flow velocity [ $\text{L T}^{-1}$ ],  $D$  is the hydrodynamic dispersion coefficient [ $\text{L}^2 \text{T}^{-1}$ ],  $t$  is time [ $\text{T}$ ],  $x$  is distance [ $\text{L}$ ], and the subscripts  $m$  and  $im$  denote the mobile and immobile domains, respectively. The relative concentration difference between the domains drives the transfer of mass

$$\theta_{im} \frac{\partial c_{im}}{\partial t} = \alpha (c_m - c_{im}) \quad [2]$$

where  $\alpha$  controls the rate of exchange between the domains [ $\text{T}^{-1}$ ]. The mass transfer rate  $\alpha$  has been derived using Fick's first law and is used to represent diffusion across a length scale (e.g., Goltz and Roberts, 1986; Parker and Valocchi, 1986; Brusseau et al., 1991, 1994):

$$\alpha = \frac{D^*}{l^2} \quad [3]$$

where  $D^*$  is the effective diffusion coefficient [ $\text{L}^2 \text{T}^{-1}$ ] and  $l$  is representative of either sphere diameter or a length scale of mixing between the two domains (e.g., Haggerty and Gorelick, 1995; Griffioen et al., 1998).

The MIM model has been applied successfully to solute transport problems using both conservative tracers and reactive tracers in a variety of hydrogeologic settings by dividing the flow field into advective-flow and no-flow regions (e.g., van Genuchten and Wierenga, 1976; Cameron and Klute, 1977; Haggerty and Gorelick, 1994; Jardine et al., 1999; Gwo et al., 2007). One of the benefits of the MIM model is that the fitting parameters  $\theta_m$ ,  $\theta_{im}$ , and  $\alpha$  may be related to and therefore constrained by porosity, particle size, diffusion coefficients, or geophysical measurements (e.g., Brusseau et al., 1994; Vanderborght et al., 1997; Casey et al., 1999; Al-Jabri et al., 2002; Lee et al., 2000; Singha et al., 2007; Luo et al., 2008; Gong et al., 2010). The assumed velocity partitioning in the MIM model into flowing and not-flowing zones is not an accurate representation of the true velocity field, however, and a single mass transfer rate fails to match BTCs with particularly long tails (e.g., Haggerty and Gorelick, 1995; Gao et al., 2009). The MIM model is a highly restricted case of the CTRW formalism described below.

The CTRW is an approach based on the conceptual picture of tracer particles undergoing a series of transitions, characterized by a distribution of transition times. The physics and geochemical mechanisms involved in the transport process, as well as the structure of the heterogeneous porous medium or nature of the flow regime, determine the relevant transition time distribution and control the interpretation of its parameters. In the CTRW framework, a solute particle undergoes a series of transitions of length  $\mathbf{s}$  and time  $t$ . Together with a master equation conserving solute mass, the random walk is developed into a transport equation in partial differential form. For a concise derivation starting from a simple random walk and leading to the transport equation, and an extensive review of the CTRW, see Berkowitz et al. (2006). The transport equation in Laplace space  $\mathcal{L}$  (denoted by a tilde  $\sim$  and Laplace variable  $u$ ) is

$$u \tilde{c}(\mathbf{s}, u) - c_o(\mathbf{s}) = -\tilde{M}(u) [v_\psi \cdot \nabla \tilde{c}(\mathbf{s}, u) - \mathbf{D}_\psi : \nabla \nabla \tilde{c}(\mathbf{s}, u)] \quad [4]$$

where

$$v_\psi = \frac{1}{t_1} \int p(\mathbf{s}) \mathbf{s} d\mathbf{s}$$

is an average tracer transport velocity [i.e., based on the first moment of the probability density function (pdf) of the transition lengths,  $p(\mathbf{s})$ , divided by a characteristic time],

$$\mathbf{D}_\psi = \frac{1}{t_1} \int \frac{1}{2} p(\mathbf{s}) \mathbf{s} \mathbf{s} d\mathbf{s}$$

is a generalized dispersion tensor, the dyadic symbol (colon) denotes a tensor product,  $c_0(\mathbf{s})$  represents the initial condition,

$$\tilde{M}(u) = t_1 u \frac{\tilde{\psi}(u)}{1 - \tilde{\psi}(u)}$$

is a “memory” function, and  $t_1$  is the characteristic transition time (Berkowitz et al., 2006, and references therein). Note that  $v_\psi$  is distinct from and therefore need not equal the average fluid flow velocity  $v_m$ ;  $v_m$  is averaged across all water particles, whereas the tracer velocity,  $v_\psi$ , is averaged across the tracer particles. We solved the one-dimensional form of Eq. [4].

The pdf  $\psi(t) = \mathcal{L}^{-1}[\tilde{\psi}(u)]$  is defined as the probability rate for a transition time  $t$  between sites. Its determination lies at the heart of the CTRW because it controls the nature of the transport. The truncated power law (TPL) form of  $\psi(t)$  has been applied successfully to a wide range of physical scenarios (Berkowitz et al., 2006); the “cut off” of the power law allows a transition from anomalous behavior to Fickian behavior at longer times. The TPL form can be written as

$$\psi(t) = \frac{n}{t_1} \frac{\exp(-t/t_2)}{[1 + (t/t_1)]^{1+\beta}}; \quad 0 < \beta < 2$$

where

$$n = \left[ \left( \frac{t_1}{t_2} \right)^\beta \exp\left(\frac{t_1}{t_2}\right) \Gamma\left(-\beta, \frac{t_1}{t_2}\right) \right]^{-1}$$

is a normalization factor,  $\beta$  is a measure of the dispersion,  $t_2$  ( $\gg t_1$ ) is a “cutoff” time, and  $\Gamma(a, x)$  is the incomplete gamma function. Note that  $\psi(t) \sim (t/t_1)^{-1-\beta}$  for  $t_1 \ll t \ll t_2$ , and decreases exponentially  $\psi(t) \sim \exp(-t/t_2)$  for  $t \gg t_2$ . Fickian transport occurs for  $\beta > 2$ , while the smaller  $\beta$  is, the more dispersive the transport. A recent study shed more light on the choice of these parameters and their interpretation in the context of flow-velocity-dependent tailing (Berkowitz and Scher, 2009). Note also that specific forms of  $\psi(t)$  can be defined for the MIM and other related models (for a detailed discussion, see Berkowitz et al., 2006).

This general concept of transport can therefore quantify a wide range of non-Fickian transport patterns. The CTRW has been applied successfully in many different settings (e.g., Berkowitz and Scher, 1998; Deng et al., 2008). Significantly, it consistently captures BTC behavior in column experiments of even well-sorted materials, where conventionally predicted classic advective–dispersive behavior does not always occur (Cortis and Berkowitz, 2004). In most cases, the transport behavior can be quantified effectively with a single

transition time distribution (Berkowitz and Scher, 2009); however, if there is clear evidence for the nature of the underlying transport mechanisms, an explicit two-scale CTRW formulation (Bijeljic et al., 2011) or a fully coupled space–time distribution may also be considered (Dentz et al., 2008).

Our understanding of the physical environment is shaped by the assumptions within our models. For example, interpretations from a MIM model assume the existence of a dual-porosity network that may or may not exist, whereas modeling the same data set with a classic ADE model may only suggest that the subsurface is highly heterogeneous. In each case, we can only infer actual behavior given concentration histories. We explored two conceptual models—CTRW and a simplified version of CTRW, the MIM model—with the goal of developing consistent interpretations of the subsurface hydrogeology.

## Field Site and Experimental Methods

### Location and Site Details

The SH-CZO is an 8-ha V-shaped catchment containing one first-order stream located in central Pennsylvania within the Valley and Ridge physiographic province of the Appalachian Mountain Front (Fig. 1). The SH-CZO is underlain almost entirely by the Silurian Rose Hill shale. The Rose Hill shale extends across much of the Appalachian Basin; locally, the Rose Hill shale is a yellow-brown, olive to blue-gray fossiliferous shale marked by well-developed fracture cleavage (Flueckinger, 1969). The resultant residual and colluvial silt loam soils are well drained and contain many shale fragments (Lin et al., 2006). Five soil series have been identified within the catchment, the Berks, Weikert, Rushtown, Blairtown, and Ernest series (Lin, 2006). Experiments were performed on

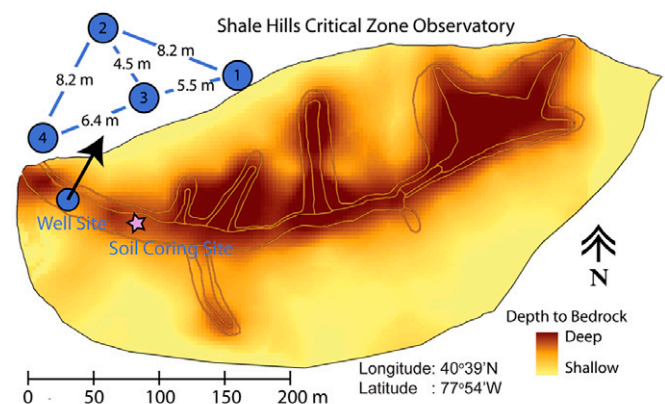


Fig. 1. The well field and soil core retrieval localities within the Shale Hills catchment (after Lin et al., 2006). Soil depth is  $>2$  m in the valley floor and  $<0.3$  m at the ridgetops. Critical Zone Monitoring Wells (CZMWs) 1, 2, and 3 are located north of the stream and CZMW 4 is located south of the stream. The field tracer test injected salt (NaBr) into CZMW 3 and extracted and sampled the tracer breakthrough at CZMW 2. Natural groundwater flow direction is approximately southwest to west.

soils retrieved from the valley bottom within the Ernest soil series, a fine-loamy, mixed, superactive, mesic Aquic Fragiudult consistent with U.S. Soil Taxonomy (Lin and Zhou, 2008). For additional details on soil distribution and descriptions, climate and hydrologic information, and geochemical composition across the catchment, see Lin (2006) and Jin et al. (2010).

We follow here the terminology introduced in Jin et al. (2011) to characterize the soil profile. The soil profile includes the regolith and saprock. Regolith is the near-surface, disaggregated, and highly altered material extending to a depth that can be reasonably sampled using a hand auger. Below this regolith lies the saprock, which is somewhat fractured and altered in place bedrock. Chemically unaltered, in place, and less-fractured shale we denote as bedrock. The soil samples for the experiments were collected in the regolith and saprock, while the field tracer experiment occurred in the transition zone between the saprock and bedrock. We found that regolith and saprock extended approximately 1 to 3 m below the land surface based on hand augering, well penetrations, and geoprobe sampling of the valley floor. Near the outlet of the catchment within the valley floor, a set of shallow boreholes (~16 m) was drilled and geophysical logs were collected in each (Fig. 2 and 3). Drilling and well log data revealed a Ca-rich slow drilling zone around 6 to 7 m below the land surface, above which was the transition between saprock and highly weathered bedrock with a comparatively high fracture density, and beneath which was a less-fractured and rather geochemically homogeneous blue-gray shale (Fig. 3). Additionally, a low natural  $\gamma$ -ray count in the upper ~7 m of the boreholes indicated a removal of clay-rich materials and deletion of the parent bedrock material (Fig. 3).

Soil core samples were collected from across the ~3-m-deep soil profile with 7.6-cm-diameter Shelby tubes, a thin-walled aluminum tube with a cutting edge on one end. Shelby tubes were hydraulically pressed into the soil using a tracked Geoprobe (Geoprobe Model 6620DT, Geoprobe Systems, Salina, KS). Because of the many rock fragments in the soil, in addition to hydraulically pressing, deeper Shelby Tubes were lightly hammered by the Geoprobe to reach the targeted soil depths. Field-sampled core lengths varied from 0.15 to 0.75 m, reaching a total depth of approximately 2.75 m. Because of the difficulty in obtaining cores due to rock fragments, poor

cohesion, and mechanical failures, we collected one sample at each depth and note that our analyses are not representative of heterogeneity within the catchment. Within 8 h of removal, samples were capped and stored in a 10°C walk-in storage cooler. An additional set of 5.08-cm-diameter samples was collected in clear acetate liners to visually inspect the soil color, texture, and particle size and composition with depth. This visual inspection helped target four separate zones that showed marked compositional differences with increased depth. This sample set provided a starting point to quantify behavior with depth.

### Physical and Hydraulic Properties

Hydraulic conductivity was measured in the intact, fixed-volume Shelby tube samples from depths of 0 to 0.2, 0.6 to 0.8, 1.6 to 1.8, and 2.3 to 2.5 m by both constant-head and falling-head

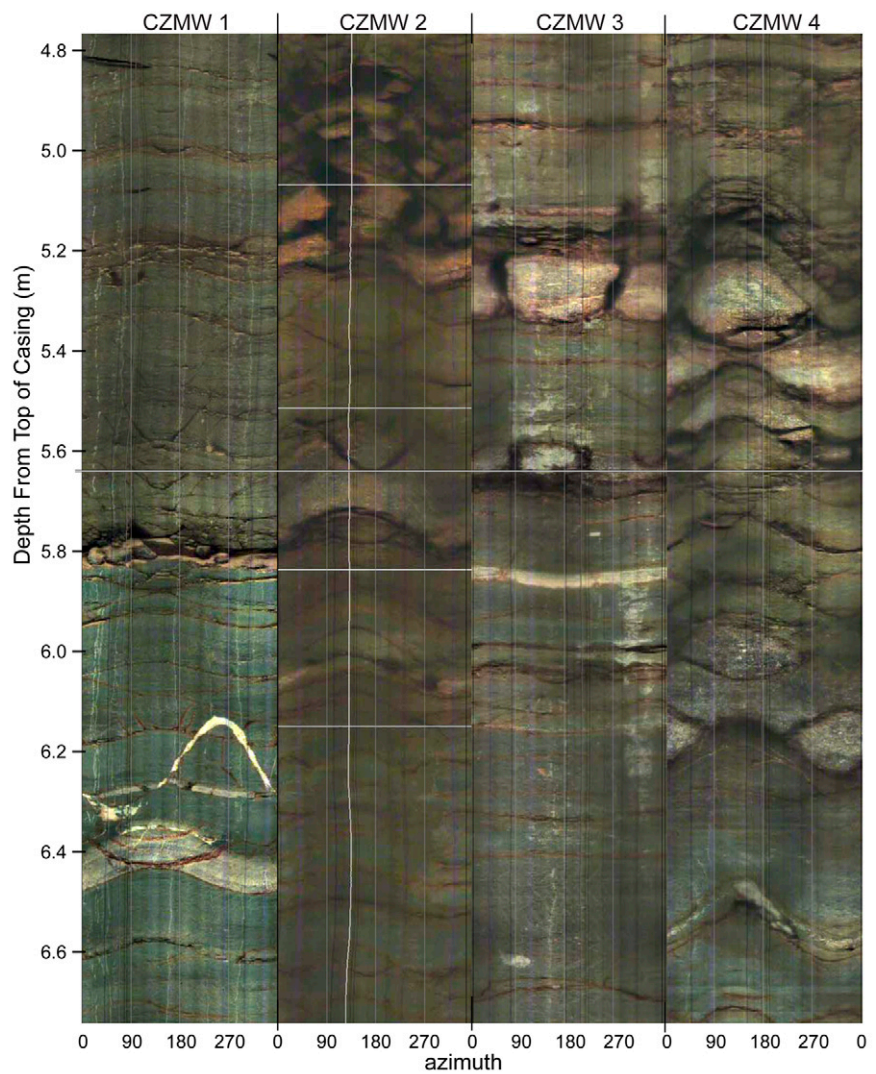


Fig. 2. Optical televiewer log of the four 16-m-deep critical zone monitoring wells (CZMWs; see Fig. 1 for location). Above approximately 6 m, the shale bedrock is olive-brown to yellow-brown, while below this depth the shale is fractured and blue-gray in color, as seen most clearly in CZMW 1. Fracturing is greatest above 6 m and decreases with depth (not seen here). The wells are cased to consolidated rock at the 2.8-m depth, so no images of the soil could be produced. These logs reveal that, on average, bedding strikes to the southwest ~230° and dips to the northwest 25 to 30°.

methods (Reynolds et al., 2002). One end of the samples was prepared with porous sintered-metal frits (bubbling pressure <20 cm) to distribute pressure evenly across the base of the sample. Total porosity was measured on 4- to 7-cm-long Shelby tube samples immediately below and adjacent to the sections used for transport experiments. Samples were fully saturated with 5 mmol L<sup>-1</sup> CaCl<sub>2</sub> under vacuum, weighed, subsequently dried at 40°C to prevent mineralogic transformation, and weighed until no resolvable change in mass occurred between measurements. Note that this drying temperature could possibly result in a lower porosity value if samples are not fully dried at the standard 105°C.

To investigate the porosity and permeability of the shale bedrock matrix, we sampled the Rose Hill shale from a nearby outcrop (~15 km northeast). Porosity was estimated by Hg porosimetry (measured by Porous Materials Inc., Ithaca, NY). Permeability was measured on the consolidated Rose Hill shale via curve matching with the transient pulse-decay method (Brace et al., 1968; Hsieh et al., 1981) in a triaxial pressure apparatus. The pressure at one end of the sample was instantaneously pulsed with 300 kPa and then allowed to equilibrate across the sample. The pressure was monitored for the decay and the increase from the pulse at the upstream and downstream sides of the sample, respectively. Theoretical curves were then matched to the data until the error was minimized.

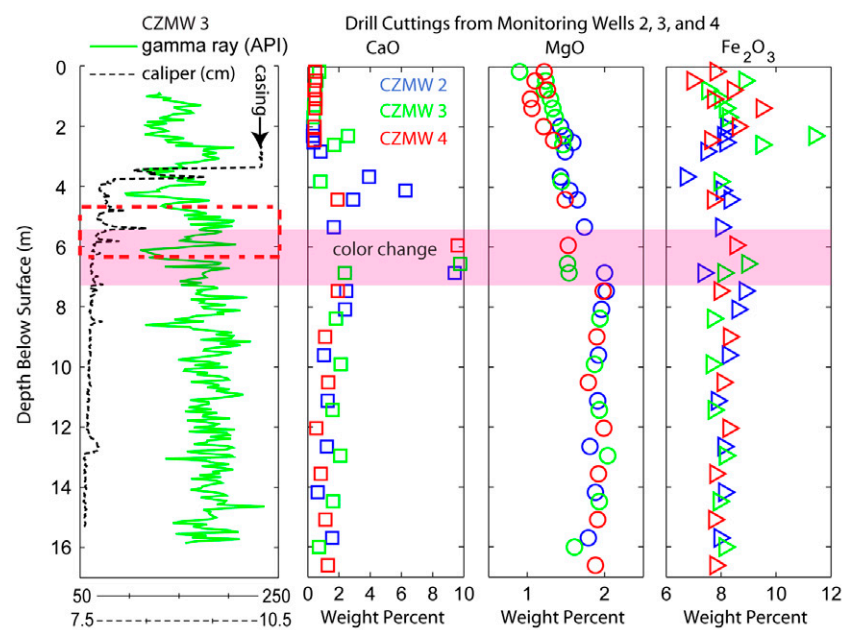


Fig. 3. Natural gamma-ray and three-arm caliper logs from Critical Zone Monitoring Well (CZMW) 3 and chemical analysis from drill cuttings from CZMWs 2, 3, and 4. Gamma curves for all four wells were collected and have a character distinctly similar to CZMW 3. A Ca-rich zone around 6 m correlates to a slow drilling zone and marks the transition between less-weathered and more-weathered shale as evidenced by (i) depletion of CaO and MgO, (ii) an increase in fracture density, and (iii) a decrease in the relative clay content as recorded by the natural gamma ray. The dashed rectangle on CZMW 3 denotes the region where the tracer was injected into the subsurface.

Particle size distribution data were analyzed on regolith and saprock from the Shelby tube samples at six depths within the soil profile. Analysis was performed by wet sieving large (>6.35 mm) and small (6.35–2.00 mm) rock fragments, sand-sized particles, and assuming that silt- and clay-sized particles comprised the remainder of the sampled material. Drill cuttings from each of the boreholes were ground and analyzed for major cation concentrations by inductively coupled plasma atomic emission spectroscopy (Penn State Materials Characterization Laboratory, University Park, PA).

## Column Tracer Experiments

Tracer experiments using SrBr<sub>2</sub> were performed on four Shelby tube core samples extracted from the soil and saprock at depths of 0 to 0.20, 0.60 to 0.80, 1.6 to 1.8, and 2.3 to 2.5 m. The Shelby tube samples were carefully cut with the aid of a low-speed band saw into 19.5 ± 0.5 cm sections from the larger field-recovered cores. Chlorinated polyvinyl chloride caps were prepared for each core by filling the convex top with an impermeable epoxy to eliminate dead volume between the sample and the cap. One brass tube fitting was fixed into the center of each cap, and the caps were secured to the sectioned Shelby tube core with adhesive; a porous sintered disk was placed at the inlet boundary between the sample and the cap to distribute the solute and pressure evenly across the sample. Fluid delivery was provided by a Masterflex L/S drive (Cole-Parmer, Vernon Hills, IL) with a six-channel pump head. To minimize solute diffusion

within the line before entering the geologic media, a three-way valve was placed at the base of the sample to switch between background influent and tracer solution.

Effluent fluid conductivity was monitored continuously by an inline conductivity meter (Model 542, Campbell Scientific, Logan, UT). The flow rate was measured regularly within a graduated cylinder as 5 mmol L<sup>-1</sup> CaCl<sub>2</sub> (fluid conductivity = 1.2 ± 0.2 mS cm<sup>-1</sup>) was pumped through the cores for several days (>30 pore volumes) until the flow rate and effluent conductivity stabilized; we chose this solution to minimize the impact of the small fraction of swelling clays (vermiculite) within the sample. The SrBr<sub>2</sub> was added to the prepared background CaCl<sub>2</sub> solution, creating a 5 mmol L<sup>-1</sup> SrBr<sub>2</sub> tracer solution (fluid conductivity = 2.3 ± 0.2 mS cm<sup>-1</sup>). Each core was saturated with three to five pore volumes of SrBr<sub>2</sub> tracer before reintroducing the background CaCl<sub>2</sub> solution. Intermittently, effluent was allowed to drip into 20-mL scintillation vials for Br<sup>-</sup> analysis. Water samples were diluted and Br<sup>-</sup> concentrations were measured on an ICS 2500 ion chromatography system (Dionex Corp., Sunnyvale, CA), using an IonPac AS18 column with an isocratic 39 mmol L<sup>-1</sup> KOH elution

program at a flow rate of  $1 \text{ mL min}^{-1}$  and an oven temperature of  $31^\circ\text{C}$ . The  $\text{Br}^-$  detection limit was  $0.05 \text{ mg L}^{-1}$ .

In this study, we analyzed only the  $\text{Br}^-$  data to examine the physical transport processes. In addition to the results presented here, tracer experiments were also attempted for soil cores from depths of 0.4 to 0.6, 1.10 to 1.31, and 2.5 to 2.75 m. These tracer experiments exhibited signs of edge effects or bypass around the sample, including nearly instantaneous first arrival of tracer and blocky or stepwise breakthrough character, and therefore these experiments were not utilized in our analysis. Replicate tracer experiments were conducted on each core that exhibited no signs of edge effects. While it is challenging to rule out the possibility of edge effects by BTC data alone, our soil extraction methods and tracer experiment setup parallel former successful studies using intact soil cores (e.g., Ward et al., 1995; Casey et al., 1999; Comegna et al., 2001; Mayes et al., 2000; Koestel et al., 2009).

### Field Tracer Test

A modified doublet tracer test was performed between Critical Zone Monitoring Well (CZMW) 3 and CZMW 2, which are 4.5 m apart (Fig. 1). The depth to water was 1 m below the land surface during the time of the tracer test. A NaBr tracer was injected at CZMW 3 below the soil into the transition between the saprock and fractured bedrock at a packed-off zone between 5 and 6 m below the land surface (Fig. 3). Extraction occurred in CZMW 2, which is cased wellbore from 0 to 2.8 m and an open wellbore from 2.8 to 10 m; the pump was placed at 9.5 m to capture tracer across the entire open borehole. The test was set up as a doublet for the first 700 min; after this period, only the extraction well was utilized. Injection of fresh water occurred for 40 min to establish steady state, followed by 150 min of saltwater injection ( $10 \text{ g L}^{-1}$  NaBr, fluid conductivity =  $14.2 \text{ mS cm}^{-1}$ ), which was followed again by freshwater injection for 550 min. Fresh water was retrieved from a local limestone and dolomite aquifer (Gatesburg formation), which has a slightly basic pH, fluid conductivity =  $300 \pm 20 \mu\text{S cm}^{-1}$ , and the dominant species include  $\text{Ca}^{2+}$ ,  $\text{Mg}^{2+}$ ,  $\text{HCO}_3^-$ ,  $\text{SO}_4^{2-}$ , and  $\text{Cl}^-$  (for more details, see Fulton et al., 2005). The injection rate was constant at  $1.7 \text{ L min}^{-1}$ . The extraction well ran continuously at  $2 \text{ L min}^{-1}$  for the entirety of the test, plus an additional 1440 min after the injection well was turned off. The natural flow gradient of 0.04 is along a bedding strike, which is nearly perpendicular to the direction of the injection–extraction well orientation (Fig. 1).

### Mobile–Immobile Solute Transport Modeling

We created a one-dimensional finite-element transport model with the MIM framework using the Earth Sciences Solute Transport module of COMSOL Multiphysics (COMSOL Inc., Burlington, MA). Initial and boundary conditions of the forward simulations were dictated by experimental conditions. Solute concentration within the mobile domain is controlled by Eq. [1] and mass is exchanged between that domain and the immobile domain by Eq.

[3]. To create an immobile pore space using COMSOL, we implemented two solute transport modules, one with a fluid velocity (Eq. [1]) and one in which the velocity and the dispersion coefficient were set to zero (Eq. [3]).

Specific discharge measurements are defined by  $q = Q/A$ , where  $Q$  is the effluent discharge [ $\text{L T}^{-1}$ ] and  $A$  is the area of the column [ $\text{L}^2$ ], which dictates the flux input to the model domain (Table 1). A Dirichlet boundary condition is used at the inlet boundary, which sets the concentration to a step function of time  $c = c(t)$ , reflecting the switch between the background solution ( $\text{CaCl}_2$ ) and tracer solution ( $\text{SrBr}_2$ ) in the mobile domain. The outlet boundary is an advective-flux condition or free boundary, which neglects transport by diffusion perpendicular to the boundary, defined by

$$\mathbf{n} \left( \theta D \frac{\partial c}{\partial x} \right) = 0$$

where  $\mathbf{n}$  is the vector normal to the boundary.

Field tracer breakthrough was modeled similarly to the columns. Flux input was estimated by calculating the advective velocity from the mean arrival time of the tracer breakthrough at the extraction well and was estimated from temporal moments. In this fractured system, the matrix hydraulic conductivity of the shale is very low ( $10^{-15} \text{ m s}^{-1}$ ), making the fractured pathways the primary controls of transport. We expected highly channelized flow and therefore assumed a channel model where the two wells are hydraulically connected by a discrete conduit (e.g., Shapiro and Nicholas, 1989), rather than a typical doublet-test flow field in a porous medium. As such, while reality is certainly more complex, we used a simple one-dimensional conceptual model that considers tracer arrival through a cross-sectional average of the domain. Similar one-dimensional assumptions are common in the fractured rock literature (e.g., Hadermann and Heer, 1996; Himmelsbach et al., 1998; Kosakowski, 2004; Novakowski et al., 2004; Goldscheider, 2008). While doublet tests in porous media tend to produce path lines with different velocities and lengths, thus producing tailing behavior that could be mistaken for mobile–immobile transport, we note here that a three-dimensional model ADE of the field site

Table 1. Physical properties of laboratory- and field-scale experiments and experimental setup.

Depth	Total porosity	Saturated hydraulic conductivity	Injection period	Flux
m		$\text{m s}^{-1}$	d	$\text{cm d}^{-1}$
0–0.2	0.44	$4.9\text{--}58 \times 10^{-7}$	0.54	66
0.6–0.8	0.34	$1.8\text{--}2.7 \times 10^{-7}$	0.45	63
1.6–1.8	0.29	$1.3\text{--}1.7 \times 10^{-8}$	0.81	29
2.3–2.5	0.29	$1.3\text{--}2.3 \times 10^{-9}$	0.58	37
5–6	–	$\sim 10^{-6}$	0.08	–
Shale	0.035	$2.7 \times 10^{-15}$	–	–

(not shown here) could not produce appropriate tailing without the inclusion of a less-mobile domain. In the presence of fracture-controlled flow, the one-dimensional conceptual model applied here provides insight into the nature of the transport behavior within this domain, although it is not in general considered “proper calibration” (Małłoszewski and Zuber, 1992). Concentrations at the outlet well were normalized to account for mass loss.

Goodness of fit to each BTC, column or field, was determined by constraining the total porosity of the model by the measured total porosity  $\theta_T \sim \theta_m + \theta_{im}$ , calculating the log-transformed RMSE, the error (%) between the measured electrical conductivity (EC) data points and model output, and plotting the solutions in log-log space to examine the tailing. To explore the range of values for the MIM solutions, we utilized the parametric sweep options in Multiphysic and performed a sensitivity analysis on the MIM model fitting parameters  $\alpha$ ,  $\theta_{im}$ , and  $\theta_m$ . The simulations chosen for the sensitivity analysis were constrained by  $\theta_T = \theta_m + \theta_{im}$ , and  $\alpha$  ranged from 0.1 to 10 d<sup>-1</sup>.

## Continuous Time Random Walk Solute Transport Modeling

For the one-dimensional CTRW model, the initial condition is  $c_r(x, t = 0) = 0$ , where  $c_r$  is the resident concentration. The inlet boundary condition is a Robin type, i.e.,

$$\tilde{c}_r(x=0, u) - \frac{D_\psi}{v_\psi} \left( \frac{\partial \tilde{c}_r}{\partial x} \right)_{x=0} = 1$$

In flux-averaged concentration terms, this boundary is also Dirichlet, as in the ADE and MIM model cases. The outlet boundary condition is a Neumann type, i.e.,  $[\partial \tilde{c}_r / \partial x]_{x=L} = 0$ .

## Results

### Porosity and Hydraulic Conductivity

Soil porosity and hydraulic conductivity both decreased from top-soil to subsoil. The uppermost soil had a  $\theta_T$  of 0.44, while deeper soils had a  $\theta_T$  of only 0.34 to 0.29 (Table 1). Hydraulic conductivity also had a decreasing trend with increased soil depth, reducing by three orders of magnitude through the soil profile (Table 1) from  $5.8 \times 10^{-6}$  m s<sup>-1</sup> at the top to  $2.3 \times 10^{-9}$  m s<sup>-1</sup> at a depth of 2.5 m. Lin (2006) also measured hydraulic conductivity on the Ernest soils down to a depth of 1.37 m, yielding hydraulic conductivity measurements between  $10^{-4}$  and  $10^{-5}$  m s<sup>-1</sup>. Values reported for weathered shale saprolite, however, commonly have hydraulic conductivities in the  $10^{-6}$  to  $10^{-9}$  m s<sup>-1</sup> range (e.g., Mayes et al., 2000). The hydraulic conductivity reported here is lower than that of Lin (2006) and probably reflects the effect of averaging because samples used in this study were about four times longer and about six times larger by volume. Hydraulic conductivity and porosimetry measurements on the consolidated Rose Hill shale matrix yielded a very low hydraulic conductivity of  $2.7 \times 10^{-15}$  m

s<sup>-1</sup> and a porosity of 0.035 (Table 1). Neuzil (1994) identified a log-linear relationship between porosity and permeability for shales and clay-rich materials from numerous laboratory data sets, and the measured porosity and permeability of the Rose Hill shale falls within the lower limits of this permeability–porosity relationship. Porosimetry data showed that only about 15% of the shale matrix is composed of pore throats >0.1 μm, with the largest 1% of the pore throats reaching 2 or 3 μm (Fig. 4). In contrast to the shale matrix, the aquifer at the SH-CZO has a high hydraulic conductivity; several slug tests and pumping tests performed in the boreholes suggest that the effective hydraulic conductivity of the aquifer is approximately  $10^{-6}$  m s<sup>-1</sup>.

Profiles observed in caliper and optical televiewer logs (Fig. 2 and 3) suggest that the primary or short-term controls on groundwater flow are secondary structures such as bedding planes, fractures, and preferential pathways rather than the low-permeability matrix. Simulating groundwater flow and transport in fractured rock provides a substantial challenge given the wide range in hydraulic conductivity across a short interval. Fracture sets typically occur as groups of tens to thousands of individual fractures, although only a small proportion of those may be relevant for conducting fluids (e.g., Long et al., 1991; Renshaw, 1995; Hsieh and Shapiro, 1996). The lack of spatial and hydrologic resolution of the fracture network at the SH-CZO limits our ability to simulate flow using a discrete fracture network.

Complicating efforts to predict solute transport in fractured media is a fundamental uncertainty regarding the physical processes at work. For example, long tails on solute BTCs can be attributed to either rate-limited mass transfer between fractures and matrix (Grisak et al., 1980; Neretnieks, 1980; Rasmuson and Neretnieks, 1986) or the existence of multiple advective pathways

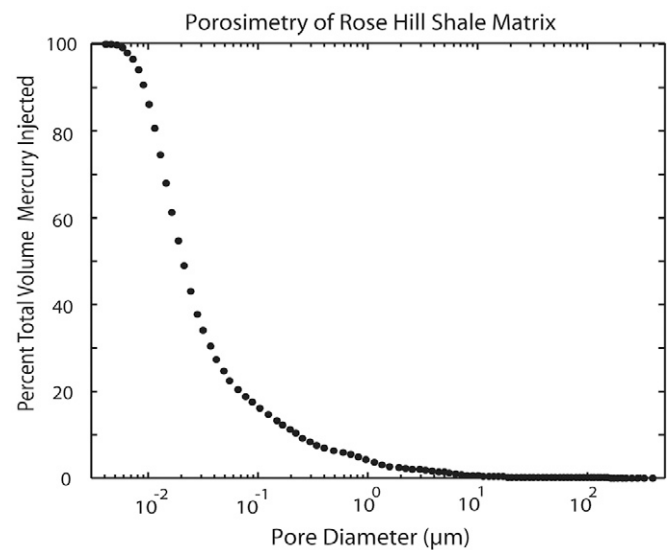


Fig. 4. Mercury porosimetry results performed on a consolidated, unfractured Rose Hill shale sample. Total calculated porosity for the sample, based on these porosimetry data, is 0.035.

of differing velocity (Becker and Shapiro, 2000, 2003). In this study, we observed that the majority of pores within the shale were  $<0.1 \mu\text{m}$  (Fig. 4), providing the capacity to store solutes but being less likely to permit advection. Assuming that diffusion controls the transfer of mass between these small pores and the adjacent advective pathways, we expect such processes could contribute to transport processes at long time scales. Macropores and preferential flow paths were also inferred from high spatially resolved soil-moisture data in the catchment (Lin, 2006). Given the large range in hydraulic conductivity, the presence of macropores, and the variability in porosity at the SH-CZO, we might expect BTCs from both the soil and aquifer to be asymmetric, having earlier than expected breakthrough times and exhibiting tailing behavior due to rate-limited mass transfer and variable or multiple advective pathways.

### Model Analysis

Figure 5 depicts the fluid EC together with  $\text{Br}^-$  concentrations in addition to ADE, MIM, and CTRW model solutions for the soil core tracer experiments. Each  $\text{Br}^-$  BTC is characterized by rapid breakthrough and tailing. The results are presented in a log-log plot, which allows detailed examination of the BTC tailing. Values for ADE, MIM, and CTRW model fitting parameters are listed in Tables 2 and 3. The MIM soil core parameters, in conjunction with soil properties, are plotted as a function of soil depth in Fig. 6. While the ADE could, in most cases, match the mean breakthrough time, it failed to match the observed tailing behavior. Additionally, the ADE consistently reached  $c/c_0 = 1$  during

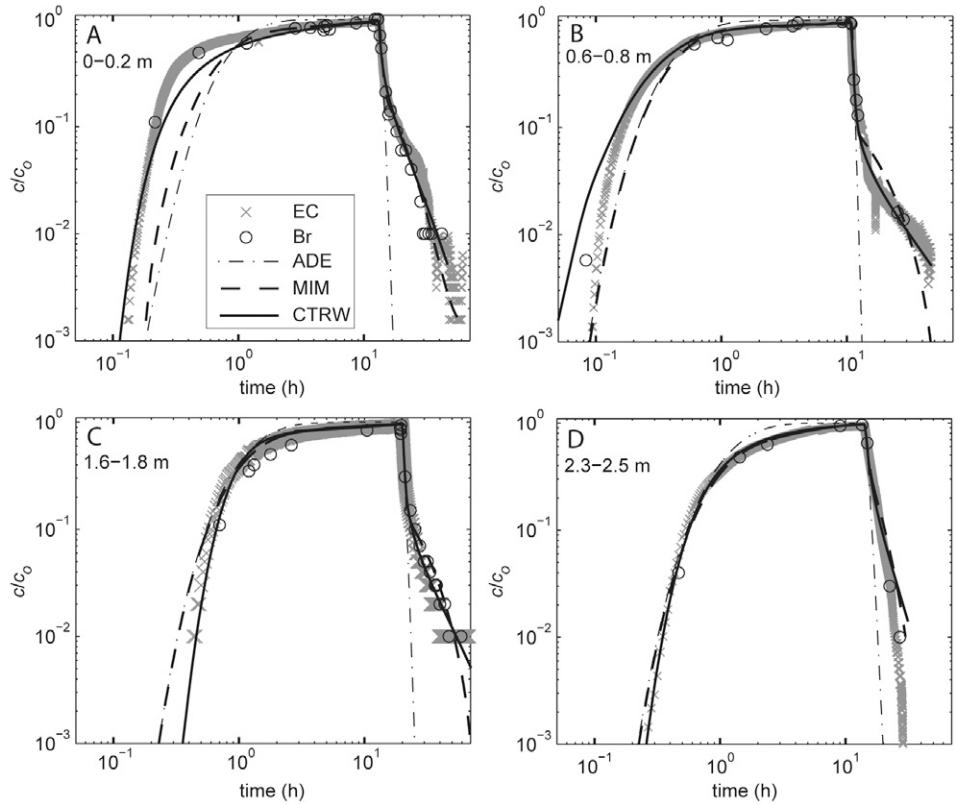


Fig. 5. Measured breakthrough curves with advection–dispersion equation (ADE), mobile–immobile (MIM) model, and continuous time random walk (CTRW) solutions for soil cores from (A) 0- to 0.2-, (B) 0.6- to 0.8-, (C) 1.6- to 1.8-, and (D) 2.3- to 2.5-m depths. EC = effluent electrical conductivity,  $\text{Br}^-$  =  $\text{Br}^-$  concentration.

breakthrough, while the observed maximum breakthrough was  $c/c_0 = 0.95 \pm 0.02$ . Therefore, the ADE was predicting an equilibrium state before we observed such a state in the measured data. Because the ADE failed to match much of the observed tracer transport behavior, we focus our analysis on the CTRW and MIM modeling results.

Figure 5A shows the results of the shallow core from a depth of 0 to 0.2 m. The breakthrough was fast and CTRW captured this behavior better than the ADE or MIM models. The tail was fit well by the

Table 2. Best-fit advection–dispersion equation (ADE) and mobile–immobile (MIM) model parameters (mobile-phase porosity,  $\theta_m$ ; immobile-phase porosity,  $\theta_{im}$ ; total porosity,  $\theta_T$ ; mass transfer rate,  $\alpha$ ) used for fitting laboratory- and field-scale data.

Depth	$\theta_m^\dagger$	$\theta_{im}$	$\theta_m/\theta_T$	$\alpha$	Dispersivity $^\dagger$
m				$\text{d}^{-1}$	m
0–0.2	0.18	0.26	0.41	1.17	0.035
0.6–0.8	0.10	0.23	0.30	0.67	0.05
1.6–1.8	0.11	0.18	0.38	0.41	0.05
2.3–2.5	0.14	0.15	0.48	1.13	0.052
Field tracer	0.045	0.08	0.36	0.30	0.50

$^\dagger$  ADE and MIM model parameters, first fit using ADE then fixed in MIM simulations and constrained to laboratory measurements.

Table 3. Best-fit continuous time random walk parameters (average tracer transport velocity,  $v_\psi$ ; generalized dispersion tensor  $\mathbf{D}_\psi$ ; dispersion measure,  $\beta$ ; characteristic transition time,  $t_1$ ; cutoff time,  $t_2$ ) used for fitting laboratory- and field-scale data.

Depth	$v_\psi$	$\mathbf{D}_\psi$	$\beta$	$t_1$	$t_2$
m	$\text{cm s}^{-1}$	$\text{cm}^2 \text{s}^{-1}$		s	d
0–0.2	$9.84 \times 10^{-2}$	$6.86 \times 10^{-3}$	0.91	3.31	1.11
0.6–0.8	$1.35 \times 10^{-1}$	$7.58 \times 10^{-1}$	1.05	$1.0 \times 10^{-3}$	9.19
1.6–1.8	$6.0 \times 10^{-2}$	$4.0 \times 10^{-2}$	1.01	$1.26 \times 10^{-2}$	3.66
2.3–2.5	$5.4 \times 10^{-2}$	$1.6 \times 10^{-2}$	0.91	2.19	0.73
Field tracer	3.35	2.87	0.83	$6.19 \times 10^{-1}$	$2.69 \times 10^3$

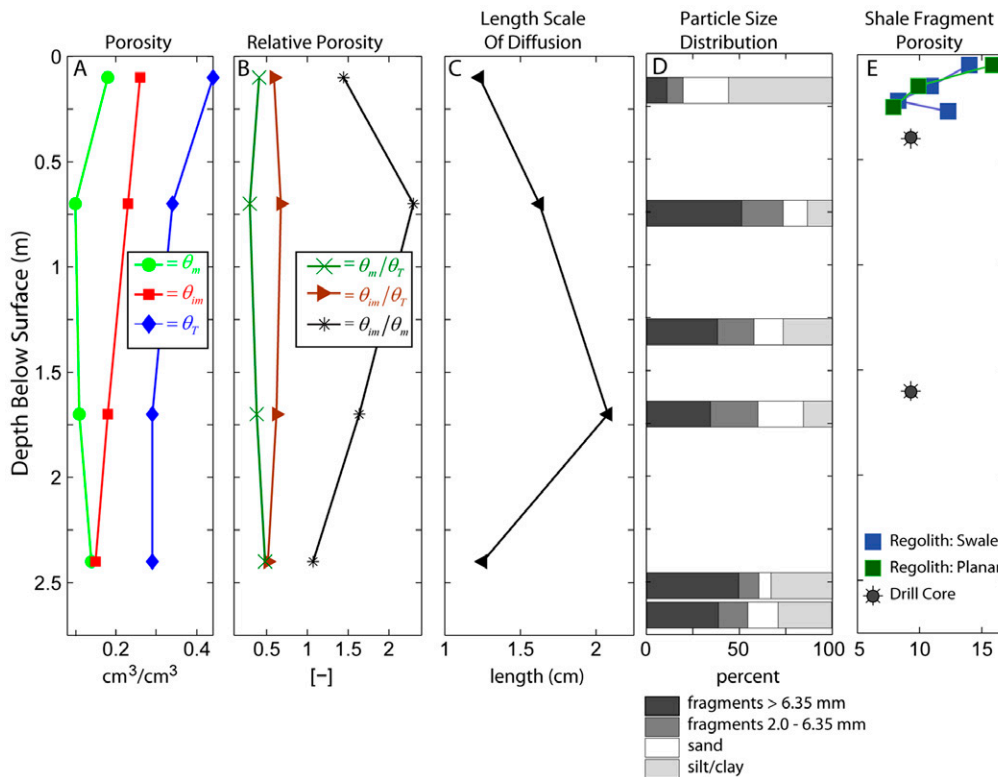


Fig. 6. Mobile-immobile modeling results plotted against soil depth, including (A) fit values for mobile and immobile porosity ( $\theta_m$ ,  $\theta_{im}$ , and  $\theta_T$  are mobile, immobile and total porosities, respectively), (B) relative porosities, (C) estimated length scale of diffusion using Eq. [3], (D) particle size distribution data from various sections in the soil profile, and (E) porosity measurements on Rose Hill shale fragments from various depths at different locations along the ridgetop of the Shale Hills Critical Zone Observatory (modified from Jin et al., 2011).

CTRW with the parameter  $\beta = 0.91$ , which indicates strong anomalous transport. The characteristic transition time  $t_1$  in this case was high, which allowed a good fit to the fast breakthrough observed. The average tracer velocity was  $\sim 50$  times faster than the measured fluid velocity. As noted below Eq. [4], the average tracer velocity may be larger or smaller than the average fluid (water) velocity. The difference between these two velocities arises because of the way that the velocities are averaged; in contrast to the definition of average fluid velocity  $v_m$ , the tracer velocity  $v_\psi$  is defined as the first moment of the transition length pdf,  $p(s)$ , divided by a characteristic time. The presence of fracturing, as in this study, can explain a tracer velocity higher than the average fluid velocity. In this case, most of the fluid flow was very slow, but a small fraction of the fluid advanced at high velocity through the fractured subsurface. Tracer injected in the vicinity of a fracture will allow most of the tracer to travel through the fracture at high velocity; these particles are excluded from low-permeability regions where water is present, yielding a much higher average velocity than that of the fluid. This difference in averaging can be considered in terms of tracer concentration, which varies throughout the domain. If the concentration is uniform throughout, then  $v_m = v_\psi$ . If the tracer concentration is higher in the high-velocity regions (e.g., tracer injection into a fracture), then  $v_\psi > v_m$ . If the tracer concentration is higher in the immobile regions (due to mass transfer), then  $v_\psi < v_m$ . Our findings are consistent with the fast breakthrough of solutes (arriving

before one pore volume) and may indicate fast channeling for solute migration in the strongly heterogeneous domain, corroborated by the relatively low  $\beta$  value.

According to the MIM model analysis, approximately 60% of the total pore space was immobile, and mass transfer between the mobile and immobile domain was fast relative to the rest of the soil cores. This shallow core deviated from the rest of the soil cores by having significant amounts of silt- and clay-sized particles containing far fewer rock fragments than deeper soil cores (Fig. 6D). The late-time tailing behavior was represented well by both MIM and CTRW models.

Data from a core from the 0.6- to 0.8-m depth are presented in Fig. 5B. The CTRW captures the early breakthrough of  $\text{Br}^-$ , which deviated slightly from the EC measurements in this case, perhaps due to dilution of the samples for the ion chromatograph during sample preparation. The CTRW best

describes the tailing shape observed in the EC record with a  $\beta$  value of 1.05. The CTRW parameters for this soil core are considerably different from the parameters for all other cores, with high solute velocity  $v_\psi$  and dispersion  $D_\psi$  values and a short transition time  $t_1$  (Table 3); these point to a transport regime controlled by fractured rock. These results are consistent with the particle size distribution (PSD) data, which indicate that  $\sim 75\%$  of the 0.6- to 0.8-m core was composed of rock fragments (Fig. 6D). The MIM model solution does not match the change in slope at  $\sim 15$  h or tailing during late time well, in contrast to the CTRW solution.

Figure 5C shows the results from the 1.6- to 1.8-m-depth core. In this case, only CTRW captures the anomalous early breakthrough as well as the long tailing, with a best-fit  $\beta$  of 1.01. The tracer velocity  $v_\psi$  is again  $\sim 50$  times greater than the flow velocity  $v_m$ , and the dispersion  $D_\psi$  falls roughly between the other dispersion values. Low mass transfer coupled with low mobile porosity is also apparent in this soil core (Fig. 6B and 6C). The significant late-time tailing behavior from this soil core was best represented by CTRW.

The BTC for the lowermost soil core does not exhibit the notable tailing observed for the intermediate soil cores but behaves more similarly to the uppermost soil core (Fig. 5D). The CTRW matches

the breakthrough portion of the curve exceptionally well, with  $v_{\psi}$ ,  $D_{\psi}$ , and  $\beta$  values similar to the 1.6- to 1.8-m soil core, while the transition time and cutoff times are quite similar to those of the uppermost soil core. The majority of the late-time tailing behavior was adequately captured by both CTRW and MIM models.

Results from the parametric sweep on the MIM model parameters  $\alpha$ ,  $\theta_{im}$ , and  $\theta_m$  for the soil cores are presented in Fig. 7. This sensitivity analysis suggests that (i) the uncertainty in the mobile and immobile porosities is larger than the uncertainty in the estimated mass transfer rates, (ii) the range of mobile–immobile porosities that result in a similar RMSE fit to the data is approximately  $\pm 0.025$  of the values reported in Table 2, and (iii) the mass transfer rates tend to reduce with depth in the 0- to 20-, 0.6- to 0.8-, and 1.6- to 1.8-m cores while increasing in the lowermost 2.3- to 2.5-m core. For the CTRW fits, the parameters (i.e., the values of  $\beta$ ,  $t_1$ , and  $t_2$  in  $\psi(t)$  and their interplay with  $v_{\psi}$  and  $D_{\psi}$ ) are all closely linked. This is because  $\psi(t)$  is based on the flow field, and thus the heterogeneity distribution, of the entire domain within the CTRW ensemble-averaged transport equation (for a detailed discussion, see Berkowitz et al., 2006). As such, while for this study the value of  $t_2$  was relatively insignificant because the transport was clearly non-Fickian, the other parameters values were indeed sensitive. Variations of as little as a few percentage points in the values reported in Table 3 led to notably poorer fits to the data.

With respect to the field-scale tracer test, the CTRW fit was notably better than the ADE and MIM model results (Fig. 8). The CTRW fitting parameters indicate a strongly anomalous transport behavior. Compared with the CTRW parameters of the core data analysis,  $\beta$  is slightly lower and  $t_2$  is significantly larger than the typical values obtained for the laboratory-scale core data, indicating the dominance of the non-Fickian nature of transport at the field scale. The inability of the MIM model to match the breakthrough portion and long tail of the field data also attests to highly non-Fickian transport.

## Implications and Discussion

The MIM modeling of the soil core tracer experiments indicated trends that mimicked those observed in the measured porosity and hydraulic conductivity in that MIM model parameters tended to decrease with increased depth. Our results suggest that (i) solutes appear to have been advecting in 30 to 50% of the total porosity across the soil profile, and (ii) the fraction of immobile pore space decreased linearly with depth (Fig. 6A). The low mobile porosity relative to the total pore space (<50%) signals the existence and control of preferential flow paths, consistent with similar MIM model analysis of undisturbed soil

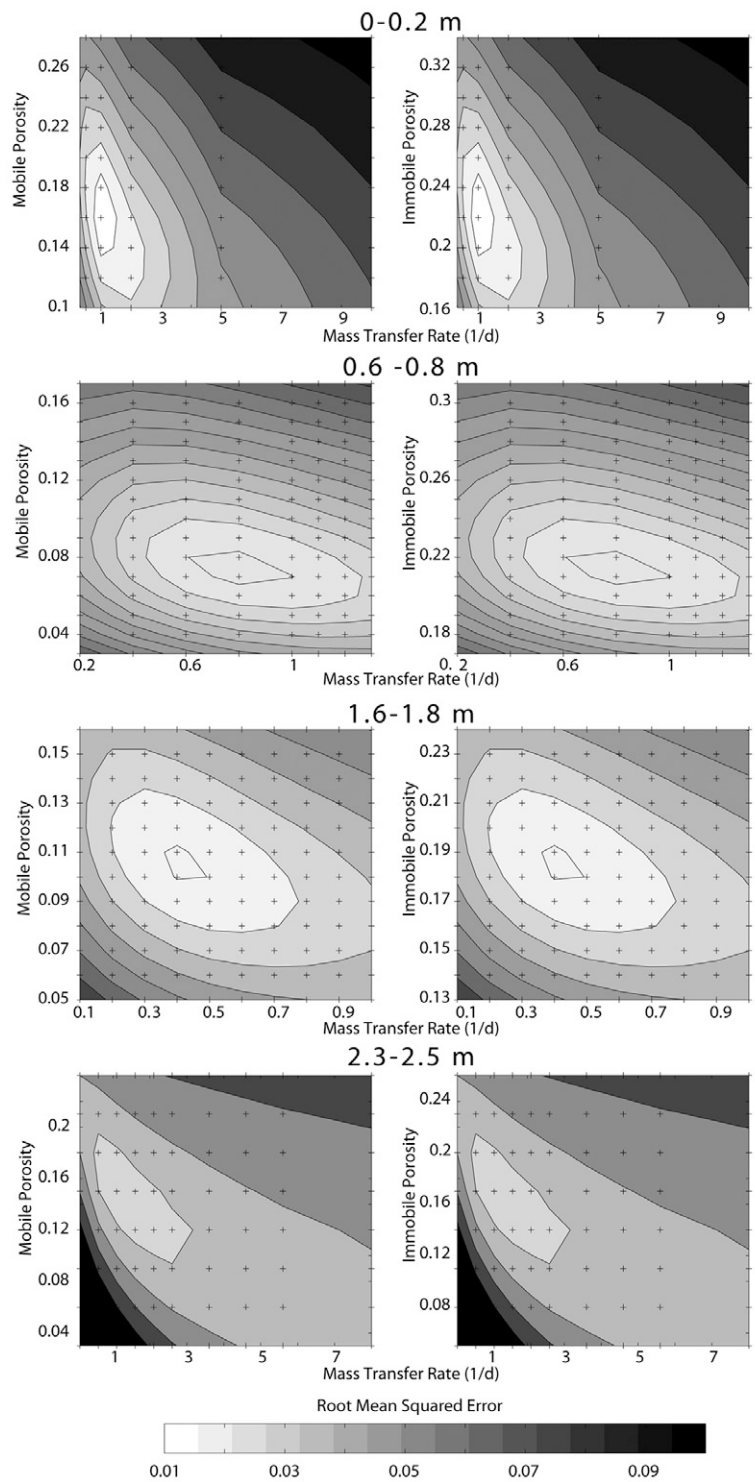


Fig. 7. Root mean square error (RMSE) results from a series of mobile–immobile model simulations for the four soil cores. Crosses represent simulated values.

cores (Seyfried and Rao, 1987). The effect of preferential flow may be especially important in the intermediate cores (0.6–0.8 and 1.6–1.8 m) where  $\theta_m/\theta_T < 0.4$ . In the regions of the soil profile dominated by rock fragments, we expected mass transfer to the less-mobile pore space to be controlled by diffusion (Griffioen et al., 1998).

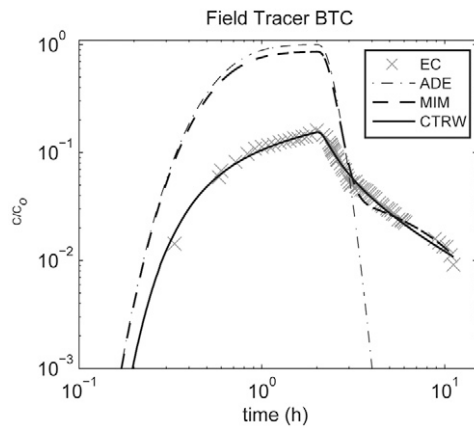


Fig. 8. Field tracer breakthrough curve (BTC) for measured effluent electrical conductivity (EC) at pumped Critical Zone Monitoring Well 2 and advection–dispersion equation (ADE), mobile–immobile (MIM) model, and continuous time random walk (CTRW) solutions.

The MIM model parameters for the soil cores may be indicative of physical properties related to weathering. The pattern of decreasing immobile porosity from shallow to deep soil cores (Fig. 6A) may be capturing the effect of increased weathering. This observation is supported by the neutron porosity work of Jin et al. (2011), which investigated the porosity of the shale fragments extending through the regolith and down into the bedrock. The porosity of the shale fragments was >15% in the uppermost soils, decreasing to ~8% at depth (Fig. 6E). Jin et al. (2011) suggested that three pore types exist within the shale bedrock: (i) interlayer pores (pores between 2:1 clay layers), (ii) intraparticle pores (pores between mineral assemblages), and (iii) interparticle pores (pores between particle boundaries), the smallest pores being the interlayer pores. The increase in shale porosity from weathering is thought to occur from the development of intraparticle pore space from the dissolution of clay minerals (Jin et al., 2011). Lower natural  $\gamma$ -ray values at the surface (1–6 m) measured in 16-m-deep boreholes near the catchment outlet attest to a reduction in clay content near the surface (Fig. 3). Above the  $\gamma$ -ray tool measurements (<1 m), we observed an increase in clay content in the 0- to 20-cm core, probably due to downslope transport and mass wasting (Fig. 6). Our modeling indicates that immobile pore space decreases with depth in the soil profile, which may be associated with the weathering of clay minerals in the shale fragments in the regolith and saprock. We cannot rule out, however, changes in the immobile pore space due to a reduction in total porosity and changes in the soil composition, texture, and PSD. We conceptualize the mobile pore space to be comprised of regions between and adjacent to the many rock fragments (preferential pathways), and some fraction of that immobile pore would be comprised of pores in the shale fragments themselves.

To examine the inferred relationship between weathering and immobile porosity, we examined the distribution of rock fragments

across the soil profile by analyzing the PSDs of the soil cores (Fig. 6D). The PSDs collected by wet sieving revealed that rock fragments comprised 20 to 50% of the total soil composition, and more than ~60% of those rock fragments were >6.35 mm. The weathering out of clay minerals results in higher porosity on the rock fragment and more connectivity within the shale fragments (Jin et al., 2011). This increase in porosity and connectivity on the shale fragments may be associated with the increased immobile porosity identified by the MIM modeling. Visual inspection revealed that rock fragments in the upper three soil cores were olive-gray to yellow and subangular to rounded, whereas fragments from a depth of 2.5 m and greater were bluish-gray and angular to subangular, with only slight visual indication of weathering. The rock fragment composition change is consistent with observations by the optical televiewer and geophysical logs, where shale bedrock changed from more weathered (saprock) to less weathered (bedrock) below the 6-m depth (Fig. 2 and 3). Soil cores from 0.6 to 0.8 and 1.6 to 1.8 m contained >60% weathered rock fragments and had relatively large immobile domains based on MIM modeling, suggesting a relationship between weathering of the shale fragments and the immobile domain porosity. Furthermore, mass balance results from the tracer experiments suggest that more mass remained in the deeper soil cores than the uppermost core. The lower mass recovery in the deeper cores with more shale fragments suggests retention of solutes in the shale-fragment-dominated media. Finally, we point out that rock fragments did not make up a large percentage of the shallow core, indicating that the structure of the immobile domain may be a combination of not only rock fragment porosity but also changes in soil texture and composition, a reduction in total porosity, and changes in the PSD with depth.

With the exception of the deepest soil core, the rate of mass transfer  $\alpha$  also decreased with depth into the soil profile and aquifer, being  $\sim 1 \text{ d}^{-1}$  in the uppermost core and  $< 1 \text{ d}^{-1}$  for soil cores from 0.6 to 0.8 and 1.6 to 1.8 m (Table 2). These mass transfer values are similar to those of Reedy et al. (1996), who also performed tracer experiments on an undisturbed shale saprolite core. A reduction in the mass transfer rate with depth might be expected if the mass transfer rate is reflecting the increased length of mixing (Eq. [3]) or the increased heterogeneity encountered by the mobile and immobile domains (Haggerty and Gorelick, 1995). The deepest soil core may break from the trend of decreasing mass transfer rate because the immobile pore space on the shale fragments is only poorly developed and therefore the mass transfer to this region is only minimal relative to the time scale of the experiment. Koch and Flüßler (1993) pointed out that simultaneously optimizing  $\theta_m$ ,  $\theta_{im}$ , and  $\alpha$  could result in highly correlated parameters that have little physical meaning. For example, it is not clear how to interpret the characteristic length scale of diffusion, as defined in Eq. [3]. The diffusion length scales estimated for the soil cores are on the order of centimeters, while >60% of the soil is composed of small rock fragments (2–6.35 mm) and sand- and silt-sized particles. The diffusion length scale may reflect the relationship

between the dead-end pore space and fracture spacing, the presence of large rock fragments, or a combination of these physical properties. We note that while it is difficult to measure many of these fitted parameters in the field directly, there is certainly correlation between physical properties and our estimated parameters. Failing to directly tie parameters such as mass transfer rates and diffusion scales directly to physical properties limits our ability to interpret solute transport behavior; however, we (i) have highlighted a potential relationship between immobile pore space and rock fragments, and (ii) validated the prevalence of preferential flow paths at four depths within the soil profile using this modeling analysis.

The CTRW provides additional interpretation of transport processes compared with the MIM model analysis above. The CTRW model fits provide a means to examine the degree of non-Fickian transport. The extent of non-Fickian transport is inferred from the parameters of  $\psi(t)$  (mainly  $\beta$ ) so that the shape of the transition rate probability, obtained by the fitting process, explains the dynamical aspects of the transport rather than offering a concrete suggestion as to the structure of the porous domain. As noted above, the heterogeneous structure of the porous medium is not the only cause of non-Fickian transport. In both soil cores and the field scale, we found anomalous early breakthrough and long tailing. The early breakthrough is consistent with the exceptionally high average solute velocity  $v_{\psi}$ , compared with the average fluid velocity  $v_m$ , which may result from the presence of strong preferential pathways. The highly anomalous nature of the transport observed by the long tailing was further confirmed by the low  $\beta$  values. Unlike the MIM model results, however, we did not find a distinct trend in the CTRW parameters with soil core depth. In all cases presented here, the parameter  $t_2$  indicated that the tracer injection experiment lay in the non-Fickian times, the power-law region of the TPL pdf, because  $t_2$  was larger than the experiment duration. When the cutoff time  $t_2$  is large, the mass transfer rate required to capture the tailing behavior is low and the goodness of the MIM model fit to the BTC diminishes (Fig. 5B, 5C, and 7). Despite contrasting properties between the soil cores at 0 to 0.2 and 2.3 to 2.5 m (Table 1), these cores showed similar CTRW-fitted parameters. This result is an interesting feature of the CTRW, which demonstrates that while media can appear to be quite different structurally, the transport behavior within them can be quite similar in terms of the extent of non-Fickian behavior, dictated by the transition rate probability  $[\psi(t)]$  parameters (for details, see, e.g., Berkowitz and Scher, 2009, 2010). This is because transport must be considered in terms of residence time and tracer interactions between “fast” and “slow” zones so that the controlling parameters are often dynamical rather than structural.

The CTRW fit the experimental data somewhat better than the MIM model and much better than the ADE in this system, but this is not simply a matter of parameterization. The CTRW has a well-defined number of parameters, whereas, e.g., the ADE

assumes an inherent Fickian transport so that the parameters needed to describe non-Fickian transport are discarded a priori. It is important to recognize that the non-Fickian nature of the tracer transport does not arise solely from mass transfer to immobile regions but also from the inherent heterogeneity of the medium and tracer residence time effects on concentration tailing that are not explicitly modeled by the MIM model. Insights regarding the overall non-Fickian behavior that arises from a combination of these mechanisms can be gained with CTRW modeling. In reality, all of these parameters vary in space, so all of these models are underparameterized. The question of “which model to choose” is often philosophical. That said, in combining the CTRW and MIM model analyses of the field tracer experiment, we conclude that solute transport in the aquifer is not well represented by classic advection and dispersion because there is prevalent non-Fickian transport. Solute transport in certain sections of the soil profile and within the aquifer indicate more complicated behavior than simple linear mass transfer between two domains, including early breakthrough and significant long tailing. In such cases, CTRW more accurately matches the BTCs than the MIM model.

Gao et al. (2009) also recognized the inadequacy of MIM modeling and the ability of CTRW to match long tails in a large column of highly heterogeneous materials. In those cases where the MIM model results were less adequate (0.6–0.8- and 1.6–1.8-m soil cores and the field tracer), we observed immobile domains that were more than 1.5 times the size of the mobile domain and mass transfer rates that were  $<1 \text{ d}^{-1}$ . This combination of low mass transfer rates, large immobile domains, and long cutoff times indicates the mass storage potential of the soil or aquifer matrix and suggests the need to incorporate more complex mass transfer processes such as a continuum of mass transfer rates. The MIM model has the capacity to fit either the early breakthrough or the tailing measured in the field but cannot fit the entire BTC with one set of parameters. The CTRW allows solutes to move separately from the fluid velocity and permits a slow release from storage via a distribution of mass transfer rates, providing a more complete representation of the solute transport behavior at the SH-CZO. Performing CTRW analysis without incorporating a MIM model analysis, however, cannot estimate the size of that storage zone (the immobile domain) or identify the time scale of mass transfer into and out of these storage zones.

The parameters considered here can, in principle, be used for transport prediction, although applying a transport model with parameters calibrated under specific conditions to the same domain with different conditions is clearly not trivial. While one usually aims for “robust” models that can be applied in many different circumstances, this is rarely attained in practice. Calibrated parameters can sometimes describe transport in a domain with different flow rates; this was demonstrated for two different domains, each with three different flow rates using a CTRW model (e.g., Berkowitz and Scher, 2009). In the data presented here, however,

there is no definitive pattern in the various model parameters with the depths of the cores, probably due to the overall heterogeneity of the domain. Application of these analyses across multiple scales is also difficult; the core experiments represent a smaller scale of heterogeneity than can be captured by the field test. The residence time of solutes is a key factor determining the degree of interaction between fast and slow zones; in this context, diffusive transfer may be more or less important at different scales, depending on the residence time. As the residence time increases, there is increased homogenization of the tracer plume between the fast and slow zones so that overall transport becomes more Fickian. Note that the relative influence of diffusion vs. advection could be further elucidated by conducting experiments at different flow rates.

Despite the complications associated with modeling these heterogeneous field systems, the CTRW and MIM modeling confirmed the heterogeneous nature of the regolith and shale-bedrock aquifer, offered insight into the nature of the flow field, and helped distinguish the operation of physical transport processes important to the SH-CZO. Failing to incorporate the variability of parameters into groundwater age or soil weathering models would lead to an underestimated residence time of solutes in the catchment because the rate-limiting step of mass transfer into and out of stagnant water regions retains solutes within the system longer than models that contain only advection and dispersion.

## Conclusions

Quantification of the operative solute transport processes at the column scale at four locations within the soil profile and at the field scale at the SH-CZO identified controls on the residence time of solutes, clarified the important role of preferential pathways in conducting fluid, and outlined how the composition of the regolith and aquifer contribute to the movement of solutes between more- and less-mobile domains. Additionally, we hypothesize that the MIM modeling results for the soil cores are indicative of soil properties and may reflect the effects of weathering on the soil profile. While the ADE can capture the mean arrival time of the BTCs, it consistently overestimated it at peak concentration. Consistent discrepancies between the ADE and all measured BTCs imply that transport at the SH-CZO cannot be solely characterized by advection and Fickian dispersion processes. Best-fit ADE models were found to require (i) a low effective porosity, and (ii) a large dispersivity value relative to the scale of the experiment.

Solute transport throughout the system cannot be ascribed solely to a simple MIM conceptualization. Solute transport in the soil and aquifer at the SH-CZO is characterized by highly non-Fickian behavior that in some cases is better described by a CTRW model than by a simple MIM model. In the presence of low mass transfer rates, large immobile domains, and long cutoff times, a continuum of mass transfer rates as described by the CTRW was needed to match the measured BTCs. With relation to geology, when the

subsurface is composed largely of shale fragments and fractured rock, the times required until Fickian behavior occurs tend to increase; applying a single mass transfer rate may be an oversimplification of the physical transport phenomenon. Moreover, allowing an average tracer velocity that is distinct from the fluid velocity permitted a match to the very early breakthrough and late-time tailing.

Conceptualizing solutes undergoing a series of transitions in space and time independent of the flow regime may prove useful to evaluate the function of the regolith at the SH-CZO. In this study, combining CTRW and MIM model results has helped investigation of the operative transport processes across a soil profile and within the fractured shale bedrock as a composite system. For example, the high tracer transport velocity  $v_{\psi}$  coupled with the low effective or mobile porosity  $\theta_m$  point to preferential flow. Similarly, long “cutoff” times  $t_2$  and low mass transfer rates  $\alpha$  point to significant tailing and extended residence times of solutes in the soil and aquifer. Analysis of the CTRW and MIM modeling results yielded alternative perspectives and subsequent interpretations of the subsurface transport regime, increasing our ability to define how solutes interact with, are transported through, and become retained within the geologic media. Without incorporating controlling features such as preferential flow, mass transfer, and distinctly high tracer transport velocities into solute transport models, we will inaccurately predict solute transport and, consequently, important processes like estimating the age of water at the SH-CZO.

## Acknowledgments

We wish to thank Laura Toran and Nate Wysocki for assistance in design and execution of the field tracer experiment. We thank Terryl Daniels for the collection and use of the well log data. We thank Andy Rathbun, Steve Swavely, Brett Carpenter, and Demian Saffer from the Penn State Rock Mechanics lab for assistance with the shale permeability experiments and Lixin Jin, Laura Liermann, and Lin Ma for assistance with geochemical data and particle size analysis. We thank Ryan Swanson for assistance with sensitivity analysis. Useful discussions with Susan Brantley, Michael Gooseff, and Richard Parizek are acknowledged. Funding for this research was provided from NSF Grants EAR-0725019 and EAR-0747629.

## References

- Adams, E.E., and L.W. Gelhar. 1992. Field study of dispersion in a heterogeneous aquifer: 2. Spatial moments analysis. *Water Resour. Res.* 28:3293–3307. doi:10.1029/92WR01757
- Al-Jabri, S., R. Horton, D.B. Jaynes, and A. Gaur. 2002. Field determination of soil hydraulic and chemical transport properties 1. *Soil Sci.* 167:353–368. doi:10.1097/00010694-200206000-00001
- Amundson, R., D.D. Richter, G.S. Humphreys, E.G. Jobbagy, and J. Gaillardet. 2007. Coupling between biota and earth materials in the critical zone. *Elements* 3:327–332. doi:10.2113/gselements.3.5.327
- Anderson, S.P., R.C. Bales, and C.J. Duffy. 2008. Critical Zone Observatories: Building a network to advance interdisciplinary study of earth surface processes. *Mineral. Mag.* 72:7–10. doi:10.1180/minmag.2008.072.1.7
- Becker, M.W., and A.M. Shapiro. 2000. Tracer transport in fractured crystalline rock: Evidence of nondiffusive breakthrough tailing. *Water Resour. Res.* 36:1677–1686. doi:10.1029/2000WR900080
- Becker, M.W., and A.M. Shapiro. 2003. Interpreting tracer breakthrough tailing from different forced-gradient tracer experiment configurations in fractured bedrock. *Water Resour. Res.* 39(1):1024. doi:10.1029/2001WR001190
- Berkowitz, B., A. Cortis, M. Dentz, and H. Scher. 2006. Modeling non-Fickian transport in geological formations as a continuous time random walk. *Rev. Geophys.* 44:RG2003. doi:10.1029/2005RG000178

- Berkowitz, B., and H. Scher. 1998. Theory of anomalous chemical transport in random fracture networks. *Phys. Rev. E* 57:5858–5869. doi:10.1103/PhysRevE.57.5858
- Berkowitz, B., and H. Scher. 2009. Exploring the nature of non-Fickian transport in laboratory experiments. *Adv. Water Resour.* 32:750–755. doi:10.1016/j.advwatres.2008.05.004
- Berkowitz, B., and H. Scher. 2010. Anomalous transport in correlated velocity fields. *Phys. Rev. E* 81:011128. doi:10.1103/PhysRevE.81.011128
- Bethke, C.M., and T.M. Johnson. 2008. Groundwater age and groundwater age dating. *Annu. Rev. Earth Planet. Sci.* 36:121–152. doi:10.1146/annurev.earth.36.031207.124210
- Bijeljic, B., S. Rubin, H. Scher, and B. Berkowitz. 2011. Non-Fickian transport in porous media with bimodal structural heterogeneity. *J. Contam. Hydrol.* 120–121:213–221. doi:10.1016/j.jconhyd.2010.05.007
- Brace, W.F., J.B. Walsh, and W.T. Frangos. 1968. Permeability of granite under high pressure. *J. Geophys. Res.* 73:2225–2236. doi:10.1029/JB073i006p02225
- Brantley, S.L., M.B. Goldhaber, and V. Ragnarsdottir. 2007. Crossing disciplines and scales to understand the critical zone. *Elements* 3:307–314. doi:10.2113/gselements.3.5.307
- Brusseau, M.L., Z. Gerstl, D. Augustijn, and P.S.C. Rao. 1994. Simulating solute transport in an aggregated soil with the dual-porosity model: Measured and optimized parameter values. *J. Hydrol.* 163:187–193. doi:10.1016/0022-1694(94)90028-0
- Brusseau, M.L., R.E. Jessup, and P.S.C. Rao. 1991. Nonequilibrium sorption of organic chemicals: Elucidation of rate-limiting processes. *Environ. Sci. Technol.* 25:134–142. doi:10.1021/es00013a015
- Cameron, D.R., and A. Klute. 1977. Convective–dispersive solute transport with a combined equilibrium and kinetic adsorption model. *Water Resour. Res.* 13:183–188. doi:10.1029/WR013i001p00183
- Casey, F.X.M., D.B. Jaynes, R. Horton, and S.D. Logsdon. 1999. Comparing field methods that estimate mobile–immobile model parameters. *Soil Sci. Soc. Am. J.* 63:800–806. doi:10.2136/sssaj1999.634800x
- Coats, K.H., and B.D. Smith. 1964. Dead-end pore volume and dispersion in porous media. *SPE J.* 4:73–84. doi:10.2118/647-PA
- Comegna, V., A. Coppola, and A. Sommella. 2001. Effectiveness of equilibrium and physical non-equilibrium approaches for interpreting solute transport through undisturbed soil columns. *J. Contam. Hydrol.* 50:121–138. doi:10.1016/S0169-7722(01)00100-0
- Cortis, A., and B. Berkowitz. 2004. Anomalous transport in “classical” soil and sand columns. *Soil Sci. Soc. Am. J.* 68:1539–1548. doi:10.2136/sssaj2004.1539
- Dane, J.H., and G.C. Topp (ed.). 2002. *Methods of soil analysis. Part 4. Physical methods.* SSSA Book Ser. 5. SSSA, Madison, WI.
- Deng, J., X. Jiang, X. Zhang, W. Hu, and J.W. Crawford. 2008. Continuous time random walk model better describes the tailing of atrazine transport in soil. *Chemosphere* 71:2150–2157. doi:10.1016/j.chemosphere.2008.01.001
- Dentz, M., H. Scher, D. Holder, and B. Berkowitz. 2008. Transport behavior of coupled continuous-time random walks. *Phys. Rev. E* 78:041110. doi:10.1103/PhysRevE.78.041110
- Dere, A., T. White, L. Jin, D. Harbor, M. Townsend, and S.L. Brantley. 2010. Shale weathering rates across a continental-scale climosequence. p. 27–30. *In* R.J. Gilkes and N. Prakongkap (ed.) *Soil solutions for a changing world: World Congr. Soil Sci., 19th, Brisbane, QLD, Australia.* 1–6 Aug. 2010. Int. Union Soil Sci., Sydney, Australia.
- Duffy, C.J. 2010. Dynamical modelling of concentration–age–discharge in watersheds. *Hydrol. Processes* 24:1711–1718. doi:10.1002/hyp.7691
- Flueckinger, L.A. 1969. *Geology of a portion of the Allensville quadrangle, Centre and Huntingdon Counties, Pennsylvania.* Rep. 176. Topogr. and Geol. Surv., Middletown, PA.
- Fulton, J.W., E.H. Koerkle, S.D. McAuley, S.A. Hoffman, and L.F. Zarr. 2005. Hydrogeologic setting and conceptual hydrologic model of the Spring Creek basin, Centre County, Pennsylvania, June 2005. *Sci. Invest. Rep.* 2005-5091. USGS, Reston, VA.
- Gao, G., H. Zhan, S. Feng, G. Huang, and X. Mao. 2009. Comparison of alternative models for simulating anomalous solute transport in a large heterogeneous soil column. *J. Hydrol.* 377:391–404. doi:10.1016/j.jhydrol.2009.08.036
- Goldscheider, N. 2008. A new quantitative interpretation of the long-tail and plateau-like breakthrough curves from tracer tests in the artesian karst aquifer of Stuttgart, Germany. *Hydrol. J.* 16:1311–1317.
- Goltz, M.N., and P.V. Roberts. 1986. Interpreting organic solute transport data from a field experiment using physical nonequilibrium models. *J. Contam. Hydrol.* 1:77–93. doi:10.1016/0169-7722(86)90008-2
- Gong, R., C. Lu, W.-M. Wu, H. Cheng, B. Gu, D.B. Watson, C.S. Criddle, P.K. Kitanidis, S.C. Brooks, P.M. Jardine, and J. Luo. 2010. Estimating kinetic mass transfer by resting-period measurements in flow-interruption tracer tests. *J. Contam. Hydrol.* 117:37–45. doi:10.1016/j.jconhyd.2010.06.003
- Goode, D.J. 1996. Direct simulation of groundwater age. *Water Resour. Res.* 32:289–296. doi:10.1029/95WR03401
- Gorelick, S.M., G. Liu, and C. Zheng. 2005. Quantifying mass transfer in permeable media containing conductive dendritic networks. *Geophys. Res. Lett.* 32:L18402. doi:10.1029/2005GL023512
- Griffioen, J.W., D.A. Barry, and J.Y. Parlange. 1998. Interpretation of two-region model parameters. *Water Resour. Res.* 34:373–384. doi:10.1029/97WR02027.
- Grisak, G.E., J.A. Pickens, and J.A. Cherry. 1980. Solute transport through fractured media: 2. Column study of fractured till. *Water Resour. Res.* 16:731–739. doi:10.1029/WR016i004p00731
- Gwo, J., M.A. Mayes, and P.M. Jardine. 2007. Quantifying the physical and chemical mass transfer processes for the fate and transport of Co(II)EDTA in a partially-weathered limestone–shale saprolite. *J. Contam. Hydrol.* 90:184–202. doi:10.1016/j.jconhyd.2006.09.013
- Hadermann, J., and W. Heer. 1996. The Grimsel (Switzerland) migration experiment: Integrating field experiments, laboratory investigations and modeling. *J. Contam. Hydrol.* 21:87–100. doi:10.1016/0169-7722(95)00035-6
- Haggerty, R., and S.M. Gorelick. 1994. Design of multiple contaminant remediation: Sensitivity to rate-limited mass transfer. *Water Resour. Res.* 30:435–446. doi:10.1029/93WR02984
- Haggerty, R., and S.M. Gorelick. 1995. Multiple-rate mass transfer for modeling diffusion and surface reactions in media with pore-scale heterogeneity. *Water Resour. Res.* 31:2383–2400.
- Himmelsbach, T., H. Hoetzel, and P. Malozewski. 1998. Solute transport in a highly permeable fault zone of Lindau Fractured Rock Test Site (Germany). *J. Ground Water* 36:792–800. doi:10.1111/j.1745-6584.1998.tb02197.x
- Hsieh, P.A., and A.M. Shapiro. 1996. Hydraulic characteristics of fractured bedrock underlying the FSE well field at the Mirror Lake site, Grafton County, New Hampshire. *In* U.S. Geol. Surv. Toxic Substances Hydrol. Progr., Proc. Tech. Mtg., Colorado Springs, CO. 20–24 Sept. 1993. *Water-Resour. Invest. Rep.* 94-4015. USGS, Reston, VA.
- Hsieh, P.A., J.V. Tracy, C.E. Neuzil, J.D. Bredehoeft, and S.E. Silliman. 1981. A transient laboratory method for determining the hydraulic properties of ‘tight’ rocks: I. Theory. *Int. J. Rock Mech. Min. Sci. Geomech. Abstr.* 18:245–252. doi:10.1016/0148-9062(81)90979-7
- Huang, K., N. Toride, and M.Th. van Genuchten. 1995. Experimental investigation of solute transport in large, homogenous and heterogeneous, saturated soil columns. *Transp. Porous Media* 18:283–302. doi:10.1007/BF00616936
- Jardine, P.M., W.E. Sanford, J.P. Gwo, O.C. Reedy, D.S. Hicks, J.S. Riggs, and W.B. Bailey. 1999. Quantifying diffusive mass transfer in fractured shale bedrock. *Water Resour. Res.* 35:2015–2030. doi:10.1029/1999WR900043
- Javaux, M., and M. Vanclooster. 2003. Scale- and rate-dependent solute transport within an unsaturated sandy monolith. *Soil Sci. Soc. Am. J.* 67:1334–1343.
- Javaux, M., and M. Vanclooster. 2004. In situ long-term chloride transport through a layered, nonsaturated subsoil. 2. Effect of layering on solute transport processes. *Vadose Zone J.* 3:1331–1339.
- Jin, L., R. Ravella, B. Ketchum, P.R. Bierman, P. Heaney, T. White, and S.L. Brantley. 2010. Mineral weathering and elemental transport during hillslope evolution at the Susquehanna/Shale Hills Critical Zone Observatory. *Geochim. Cosmochim. Acta* 74:3669–3691. doi:10.1016/j.gca.2010.03.036
- Jin, L., G. Rother, D.R. Cole, D.F.R. Mildner, C.J. Duffy, and S.L. Brantley. 2011. Characterization of deep weathering and nanoporosity development in shale—A neutron study. *Am. Mineral.* 96:498–512. doi:10.2138/am.2011.3598.
- Kazemi, G.A., J.H. Lehr, and P. Perrochet. 2006. *Groundwater age.* John Wiley & Sons, Hoboken, NJ.
- Koch, S., and H. Flüßler. 1993. Solute transport in aggregated porous media: Comparing model independent and dependent parameter estimation. *Water Air Soil Pollut.* 68:275–289. doi:10.1007/BF00479408
- Koestel, J., J. Vanderborght, M. Javaux, A. Kemna, A. Binley, and H. Vereecken. 2009. Noninvasive 3-D transport characterization in a sandy soil using ERT: 1. Investigating the validity of ERT-derived transport parameters. *Vadose Zone J.* 8:711–722.
- Kosakowski, G. 2004. Anomalous transport of colloids and solutes in a shear zone. *J. Contam. Hydrol.* 72:23–46. doi:10.1016/j.jconhyd.2003.10.005
- Lee, J., R. Horton, and D.B. Jaynes. 2000. A time domain reflectometry method to measure immobile water content and mass exchange coefficient. *Soil Sci. Soc. Am. J.* 64:1911–1917. doi:10.2136/sssaj2000.6461911x
- Lin, H.S. 2006. Temporal stability of soil moisture spatial pattern and subsurface preferential flow pathways in the Shale Hills catchment. *Vadose Zone J.* 5:317–340. doi:10.2136/vzj2005.0058
- Lin, H.S., W. Kogelmann, C. Walker, and M.A. Bruns. 2006. Soil moisture patterns in a forested catchment: A hydrogeological perspective. *Geoderma* 131:345–368. doi:10.1016/j.geoderma.2005.03.013
- Lin, H.S., and X. Zhou. 2008. Evidence of subsurface preferential flow using soil hydrologic monitoring in the Shale Hills catchment. *Eur. J. Soil Sci.* 59:34–49. doi:10.1111/j.1365-2389.2007.00988.x

- Long, J.C.S., K. Karasaki, A. Davey, J. Peterson, M. Landsfeld, J. Kemeny, and S. Martel. 1991. An inverse approach to the construction of fracture hydrology models conditioned by geophysical data: An example from the validation exercises at the Stripa Mine. *Int. J. Rock Mech. Min. Sci. Geomech. Abstr.* 28:121–142. doi:10.1016/0148-9062(91)92162-R
- Luo, J., W. Wu, J. Carley, M.N. Fienen, H. Cheng, D. Watson, C.S. Criddle, P.M. Jardine, and P.K. Kitanidis. 2008. Estimating first-order reaction rate coefficient for transport with nonequilibrium linear mass transfer in heterogeneous media. *J. Contam. Hydrol.* 98:50–60. doi:10.1016/j.jconhyd.2008.03.002
- Małozewski, P., and A. Zuber. 1992. On the calibration and validation of mathematical models for the interpretation of tracer experiments in groundwater. *Adv. Water Resour.* 15:47–62. doi:10.1016/0309-1708(92)90031-V
- Maraqqa, M.A., R.B. Wallace, and T.C. Voice. 1997. Effects of degree of water saturation on dispersivity and immobile water in sandy soil columns. *J. Contam. Hydrol.* 25:199–218. doi:10.1016/S0169-7722(96)00032-0
- Mayes, M.A., P.M. Jardine, I.L. Larsen, S.C. Brooks, and S.E. Fendorf. 2000. Multispecies transport of metal-EDTA complexes and chromate through undisturbed columns of weathered fractured saprolite. *J. Contam. Hydrol.* 45:243–265. doi:10.1016/S0169-7722(00)00108-X
- Neretnieks, I. 1980. Diffusion in the rock matrix: An important factor in radionuclide migration? *J. Geophys. Res.* 85:4379–4397. doi:10.1029/JB085iB08p04379
- Neuzil, C.E. 1994. How permeable are clays and shales? *Water Resour. Res.* 30:145–150. doi:10.1029/93WR02930
- Novakowski, K.S., G. Bickerton, and P. Lapcevic. 2004. Interpretation of injection-withdrawal tracer experiments conducted between two wells in a large single fracture. *J. Contam. Hydrol.* 73:227–247. doi:10.1016/j.jconhyd.2004.02.001
- Parker, J.C., and A.J. Valocchi. 1986. Constraints on the validity of equilibrium and first-order kinetic transport models in structured soils. *Water Resour. Res.* 22:399–407. doi:10.1029/WR022i003p00399
- Perfect, E., M.C. Sukop, and G.R. Hasler. 2002. Prediction of dispersivity for undisturbed soil columns from water retention parameters. *Soil Sci. Soc. Am. J.* 66:696–701. doi:10.2136/sssaj2002.0696
- Rasmuson, A., and I. Neretnieks. 1986. Radionuclide transport in fast channels in crystalline rock. *Water Resour. Res.* 22:1247–1256. doi:10.1029/WR022i008p01247
- Reedy, O.C., P.M. Jardine, G.V. Wilson, and H.M. Selim. 1996. Quantifying the diffusive mass transfer of nonreactive solutes in columns of fractured saprolite using flow interruption. *Soil Sci. Soc. Am. J.* 60:1376–1384. doi:10.2136/sssaj1996.03615995006000050012x
- Reilly, T.E., L.N. Plummer, P.J. Phillips, and E. Busenberg. 1994. The use of simulation and multiple environmental tracers to quantify groundwater flow in a shallow aquifer. *Water Resour. Res.* 30:421–433. doi:10.1029/93WR02655
- Renshaw, C.E. 1995. On the relationship between mechanical and hydraulic apertures in rough-walled fractures. *J. Geophys. Res.* 100:24629–24636. doi:10.1029/95JB02159
- Reynolds, W.D., D.E. Elrick, E.G. Youngs, A. Amoozegar, H.W.G. Boutilink, and J. Bouma. 2002. Saturated and field-saturated water flow parameters. p. 797–877. *In* J.H. Dane and G.C. Topp (ed.) *Methods of soil analysis. Part 4. Physical methods.* SSSA Book Ser. 5. SSSA, Madison, WI.
- Seyfried, M.S., and P.S.C. Rao. 1987. Solute transport in undisturbed columns of an aggregated tropical soil: Preferential flow effects. *Soil Sci. Soc. Am. J.* 51:1434–1444. doi:10.2136/sssaj1987.03615995005100060008x
- Shapiro, A.M., and J.R. Nicholas. 1989. Assessing the validity of the channel model of fracture aperture under field conditions. *Water Resour. Res.* 25:817–828.
- Silliman, S.E., and E.S. Simpson. 1987. Laboratory evidence of the scale effect in dispersion of solutes in porous media. *Water Resour. Res.* 23:1667–1673. doi:10.1029/WR023i008p01667
- Singha, K., F. Day-Lewis, and J.W. Lane, Jr. 2007. Geoelectrical evidence of bicontinuum transport in groundwater. *Geophys. Res. Lett.* 34:L12401. doi:10.1029/2007GL030019
- Vanderborght, J., D. Mallants, M. Vanclooster, and J. Feyen. 1997. Parameter uncertainty in the mobile-immobile solute transport model. *J. Hydrol.* 190:75–101. doi:10.1016/S0022-1694(96)03064-8
- Vanderborght, J., and H. Vereecken. 2007. Review of dispersivities for transport modeling in soils. *Vadose Zone J.* 6:29–52. doi:10.2136/vzj2006.0096
- van Genuchten, M.Th., and P.J. Wierenga. 1976. Mass transfer studies in sorbing porous media: I. Analytical solutions. *Soil Sci. Soc. Am. J.* 40:473–480. doi:10.2136/sssaj1976.03615995004000040011x
- Varni, M., and J. Carrera. 1998. Simulation of groundwater age distributions. *Water Resour. Res.* 34:3271–3281. doi:10.1029/98WR02536
- Ward, A.L., R.G. Kachanoski, A.P. von Bertoldi, and D.E. Elrick. 1995. Field and undisturbed-column measurements for predicting transport in unsaturated layered soil. *Soil Sci. Soc. Am. J.* 59:52–59. doi:10.2136/sssaj1995.03615995005900010008x